Image-based Q tomography using reverse time Q migration

Yi Shen and Tieyuan Zhu

ABSTRACT

We have developed a technique to tomographically estimate a Q model from migrated images using two-way wavefield continuation. When compared with our previously proposed technique that uses a one-way downward-continuation method, this technique better handles steep structures, e.g. salt flanks. Numerical results on a complex model with a salt body demonstrate the effectiveness of our two-way method for resolving attenuation in the presence of steep and overturned structures.

INTRODUCTION

Attenuation, parameterized by the seismic quality factor, Q, has considerable impact on surface seismic reflection data. It degrades the image quality by lowering the amplitude of events, distorting the phase of wavelet, removing the higher frequencies, and dispersing the velocity. These effects complicate reservoir interpretation. Therefore it is important to estimate the properties of this attenuation parameter and to use them for compensating the attenuated image.

Shen et al. (2013) and Shen et al. (2014) presented a new method, wave-equation migration Q analysis (WEMQA), to produce a reliable Q model. This method used one-way wavefield continuation to first migrate the viscoacoustic data with Q compensation for measuring the Q effects and then back-project these effects to update the current Q model. This method works well with gentle horizontal variations. However, the one-way method has limited abilities to represent the actual wave propagation around steep structures, because propagating the wavefield along only one direction of the depth axis cannot properly deal with overturned events. In some situations, overturned events provide extremely useful information, e.g. reservoir properties along a salt flank. In principle, two-way wavefield continuation is capable of modeling these overturned waves. Therefore, we apply two-way wavefield continuation migration with Q compensation (i.e. reverse time migration with Q compensation) to produce an image for Q-effect measurements (Zhu et al., 2014) and update the Q model using a two-way wave-equation tomographic operator to better handle the steep structures.

In this report, we first describe the theory of two-way migration with Q compensation and our two-way wave-equation tomographic operator. Then, we apply

WEMQA with this method to a complex model with a salt body to demonstrate the effectiveness of the two-way method to resolve steep structures.

THEORY

We incorporate reverse time migration with Q compensation (Zhu et al., 2014) and two-way wave-equation tomographic operator into WEMQA (Shen et al., 2013, 2014) to estimate Q model and compensate Q effects.

Reverse time migration with Q compensation

Zhu and Harris (2014) first introduced the time-domain viscoacoustic wave equation based on the constant Q model (Kjartansson, 1979), which takes the form

$$\left(\eta\mathbf{L}+\tau\mathbf{H}\frac{d}{dt}-v^{-2}\frac{\partial^2}{\partial t^2}\right)P(t)=f(t), \tag{1}$$

where t is time, P is the propagated wavefield, and f is the source wavefield, v is the acoustic velocity at the reference frequency ω_0. Operators $\mathbf{L}=(-\nabla^2)^{\gamma+1}$ and $\mathbf{H}=(-\nabla^2)^{\gamma+1/2}$ are fractional Laplacians, where the variable γ is defined as $\gamma=1/\pi\tan^{-1}(1/Q)$. The first term on the left side of Equation 1 is related to dispersion effects, and the middle term on the left side of Equation 1 is related to the absorption effects (Zhu et al., 2014). The absorption and dispersion coefficients are given by $\eta=-v^{2\gamma}\omega_0^{-2\gamma}\cos\pi\gamma$ and $\tau=-v^{2\gamma-1}\omega_0^{-2\gamma}\sin\pi\gamma$. We use a pseudo-spectral method in our numerical implementation.

Attenuation damps the higher frequencies more than the lower frequencies of the propagating wave. Compensation through Q migration (Zhu et al., 2014), i.e. the inverse of forward wave propagation, therefore preferentially boosts higher frequencies. Such amplification may gain high frequency noise and make these frequencies dominate the image. Therefore, we add a low-pass filter to help mitigate high-frequency noise artifacts in migration:

$$\left(\nabla^2+\mathbf{N}(\eta\mathbf{L}-\nabla^2)+\mathbf{N}\tau\mathbf{H}\frac{d}{dt}-v^{-2}\frac{\partial^2}{\partial t^2}\right)P(t)=f(t), \tag{2}$$

where $\mathbf{N}$ is the low-pass filter in the spatial frequency domain.

Two-way wave-equation tomographic operator

Image-based wave-equation Q tomography is a nonlinear inversion process that aims to find the Q model that minimizes the residual field in the image space, $\Delta I(\mathbf{x},\mathbf{h})$.

This residual image can be approximated by a linearized operator applied to the model perturbation ΔQ:

$$\Delta I\left(\mathbf{x},\mathbf{h}\right)=\sum_{\mathbf{y}}\frac{\partial I\left(\mathbf{x},\mathbf{h}\right)}{\partial Q\left(\mathbf{y}\right)}\mid_{Q_0}\Delta Q\left(\mathbf{y}\right), \tag{3}$$

where $\mathbf{x}$ and $\mathbf{y}$ are the coordinates of the image and model, respectively. $\mathbf{h}$ is the subsurface offset and Q_0 is the background quality factor. The adjoint of this tomographic operator projects the image perturbation back into the Q model space. The back-projected changes in the model space are used as gradient directions to conduct a line search in an optimization scheme. This back-projection can be expressed as follows:

$$\Delta Q\left(\mathbf{y}\right)=\sum_{\mathbf{y}}\left(\frac{\partial I\left(\mathbf{x},\mathbf{h}\right)}{\partial Q\left(\mathbf{y}\right)}\mid_{Q_0}\right)^{*}\Delta I\left(\mathbf{x},\mathbf{h}\right) \tag{4}$$

The derivative of $I\left(\mathbf{x},\mathbf{h}\right)$ with respect to Q is the sum of the attenuation-induced perturbed source wavefield multiplied by the background receiver wavefield and the attenuation-induced perturbed receiver wavefield multiplied by the background source wavefield:

$$\begin{aligned}&\frac{\partial I\left(\mathbf{x},\mathbf{h}\right)}{\partial Q\left(\mathbf{y}\right)}\mid_{Q_0}\\&=\sum_{\mathbf{x_s},\mathbf{x_r}}\left(\frac{\partial G\left(\mathbf{x}-\mathbf{h},\mathbf{x_s};Q_0\right)}{\Delta Q\left(\mathbf{y}\right)}\right)^{*}G^{*}\left(\mathbf{x}+\mathbf{h},\mathbf{x_r};Q_0\right)d\left(\mathbf{x_r},\mathbf{x_s}\right)\\&+\sum_{\mathbf{x_s},\mathbf{x_r}}G^{*}\left(\mathbf{x}-\mathbf{h},\mathbf{x_s};Q_0\right)\left(\frac{\partial G\left(\mathbf{x}+\mathbf{h},\mathbf{x_r};Q_0\right)}{\Delta Q\left(\mathbf{y}\right)}\right)^{*}d\left(\mathbf{x_r},\mathbf{x_s}\right),\end{aligned} \tag{5}$$

where $\mathbf{x_s}$ and $\mathbf{x_r}$ are the source and receiver coordinates respectively, G is the Green's function, and d are the surface data. The attenuation-induced perturbed wavefield can be linearized using a Taylor expansion as follows:

$$\begin{aligned}&\frac{\partial G\left(\mathbf{x},\mathbf{x_s};Q_0\right)}{\partial Q\left(\mathbf{y}\right)}\\&=-\frac{\partial\eta\left(\mathbf{y};Q\right)\mathbf{L}\left(\mathbf{y};Q\right)}{\partial Q\left(\mathbf{y}\right)}\mid_{Q_0}G\left(\mathbf{y},\mathbf{x_s};Q_0\right)G\left(\mathbf{x},\mathbf{y};Q_0\right)\\&-\frac{\partial\tau\left(\mathbf{y};Q\right)\mathbf{H}\left(\mathbf{y};Q\right)}{\partial\gamma}\mid_{Q_0}\frac{d}{dt}G\left(\mathbf{y},\mathbf{x_s};Q_0\right)G\left(\mathbf{x},\mathbf{y};Q_0\right)\\&\frac{\partial G\left(\mathbf{x},\mathbf{x_r};Q_0\right)}{\partial Q\left(\mathbf{y}\right)}\\&=-\frac{\partial\eta\left(\mathbf{y};Q\right)\mathbf{L}\left(\mathbf{y};Q\right)}{\partial Q\left(\mathbf{y}\right)}\mid_{Q_0}G\left(\mathbf{y},\mathbf{x_r};Q_0\right)G\left(\mathbf{x},\mathbf{y};Q_0\right)\\&-\frac{\partial\tau\left(\mathbf{y};Q\right)\mathbf{H}\left(\mathbf{y};Q\right)}{\partial\gamma}\mid_{Q_0}\frac{d}{dt}G\left(\mathbf{y},\mathbf{x_r};Q_0\right)G\left(\mathbf{x},\mathbf{y};Q_0\right)\end{aligned} \tag{6}$$

where:

$$\begin{aligned}
&\frac{\partial \eta\left(\mathbf{y};Q\right)\mathbf{L}\left(\mathbf{y};Q\right)}{\partial Q\left(\mathbf{y}\right)}\mid_{Q_0}\\
&=-\frac{\left(2\eta\ln v-2\eta\ln\omega_0-\pi v\tau\right)\mathbf{L}+\eta\mathbf{L}\ln\left(-\nabla^2\right)}{\pi\left(Q_0^2+1\right)}\\
&\frac{\partial \tau\left(\mathbf{y};Q\right)\mathbf{H}\left(\mathbf{y};Q\right)}{\partial \gamma}\mid_{Q_0}\\
&=-\frac{\left(2\tau\ln v-2\tau\ln\omega_0+\pi v^{-1}\eta\right)\mathbf{H}+\tau\mathbf{H}\ln\left(-\nabla^2\right)}{\pi\left(Q_0^2+1\right)}.
\end{aligned} \tag{7}$$

NUMERICAL RESULTS

Our numerical example employs a dataset generated by Schlumberger (Cavalca et al., 2013) using a 2D viscoacoustic version of the 2004 BP benchmark model (Billette and Brandsberg-Dahl, 2005). An attenuation model was added by Schlumberger to the original 2004 BP models. This Q model is not released, but its location and value has been shown by Schlumberger (Cavalca et al., 2013). The attenuation model is a space- and depth-variant absorption model made of several Q heterogeneities and a nonattenuative background (1/Q = 0.0002). To test the effectiveness of our method on the steep structure, we only focus our work on the salt region, which has a large attenuative zone (1/Q = 0.02) near the left of the salt flank. A velocity model for this region is shown in Figure 1. The viscoacoustic surface seismic data generated by Schlumberger used a finite-difference modeling code based on standard linear solid theory. In my example, 248 shots are used with 100 m spacing, and the offsets range from -15,000 m to 15,000 m. Receivers are distributed on both sides of each shot at an increment of 25 m. The cut-off frequency that we used to filter out the noise in the reverse-time migration was 30 Hz, which is 60% of the maximum useful frequency. The workflow used in this numerical example has been presented by Shen et al. (2013, 2014).

Figures 2 and 3 are the attenuated images from the viscoacoustic data using one-way and two-way Q migration with a nonattenuating model, respectively. The results show that the events beside the salt flank are attenuated in terms of the amplitude dimming, incoherency of the events, and stretching of the wavelets. Both migrations image the structure with gentle horizontal variation well. However, Figure 2 shows a poorer image around the salt flank when compared with Figure 3. The salt flank in Figure 2 is not focused. The regions beside the salt have discontinuous events and are contaminated with high-frequency noises. Figure 3 shows a sharper and clearer salt flank. The image around the salt is cleaner with less high-frequency noise and the events are more coherent.

The next step is to invert for the Q model besides the salt flank from these attenuated images using the wave-equation migration Q analysis developed by Shen et al. (2013, 2014). The initial model for the inversion has no attenuation. We analyze the attenuation effects by calculating the slope of the logarithm of the spectral ratio

between the windowed events of each trace and the events in the reference window at the same depth. The window size is 1500 m, and 100 sliding windows are used for each trace. The reference trace is the one at 24,000 m. Figure 5 and Figure 6 are the inverted Q model using one-way and two-way WEMQA, respectively. Figure 5 fails to resolve the Q model in area besides the salt flank, because one-way propagation is not able to accurately reflect the steep structure. Figure 6 shows that a two-way method retrieves the Q model in the reservoir region beside the salt well; especially at the upper part of the salt flank, which matches well with the true Q model. However, it still fails to update the Q model at the lower part of the salt flank because of the high-frequency image artifacts at that area. Figure 4 is the image using two-way migration with the inverted Q model shown in Figure 6 for compensation. The results show that the image at the lower region is not well compensated because of the weak updating of the Q model there. Therefore, a filter, e.g. a curvelet-transform-based filter, is needed to mitigate the image noise. But, the events in the rest of the part beside the salt flank are compensated. Their amplitudes are partially recovered, events are more coherent, and phases are corrected.

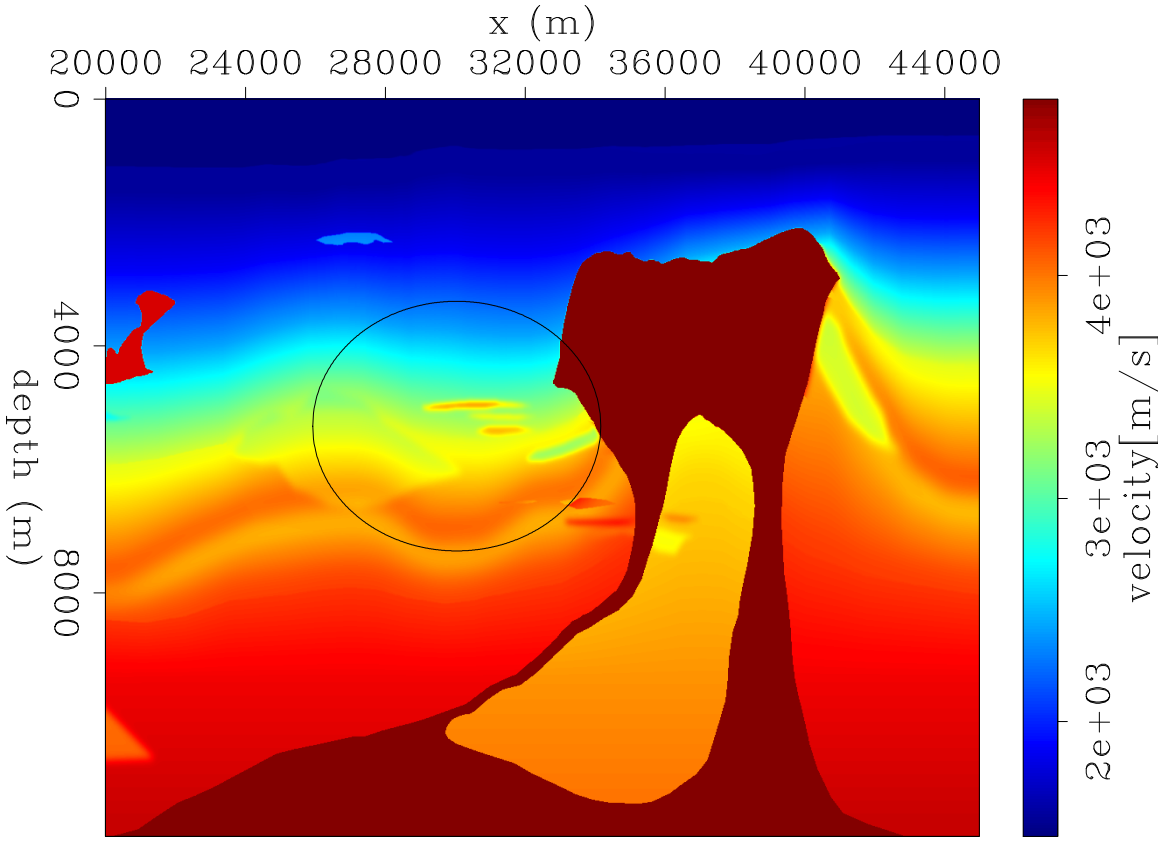

Figure 1: BP velocity model. The circles approximately show the location of the attenuation zone besides the salt flank, with the lowest Q value of $Q = 50$. [**ER**]

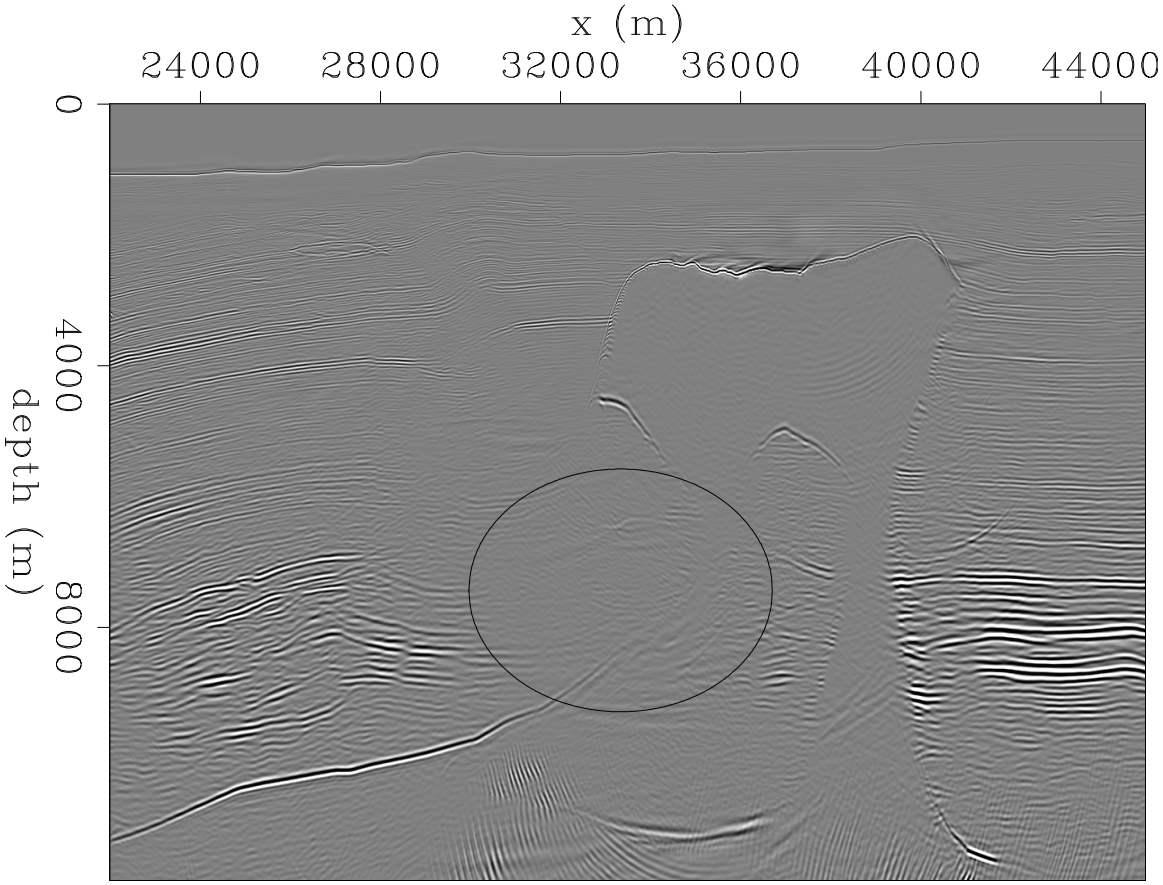

Figure 2: Attenuated images from the viscoacoustic data using one-way Q migration with a nonattenuating model. As shown in the circles, the salt flank is not focused, and the regions beside the salt have discontinued events and are contaminated with high-frequency noises. [**CR**]

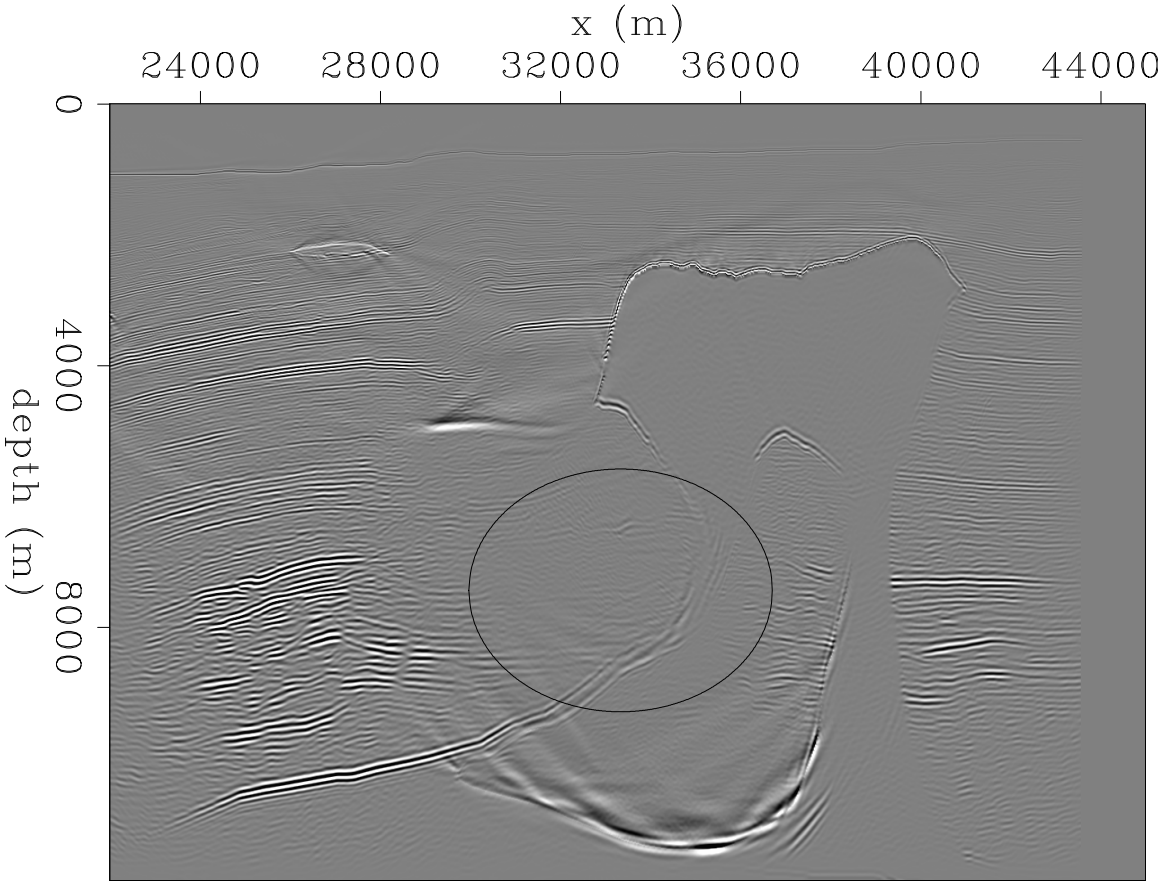

Figure 3: Attenuated images from the viscoacoustic data using two-way reverse-time Q migration with nonattenuating model. As shown in the circles, the salt flank is sharp and well-focused. The image around the salt is cleaner with less high-frequency noises, and the events becomes more coherent, when compared with Figure 2. [**CR**]

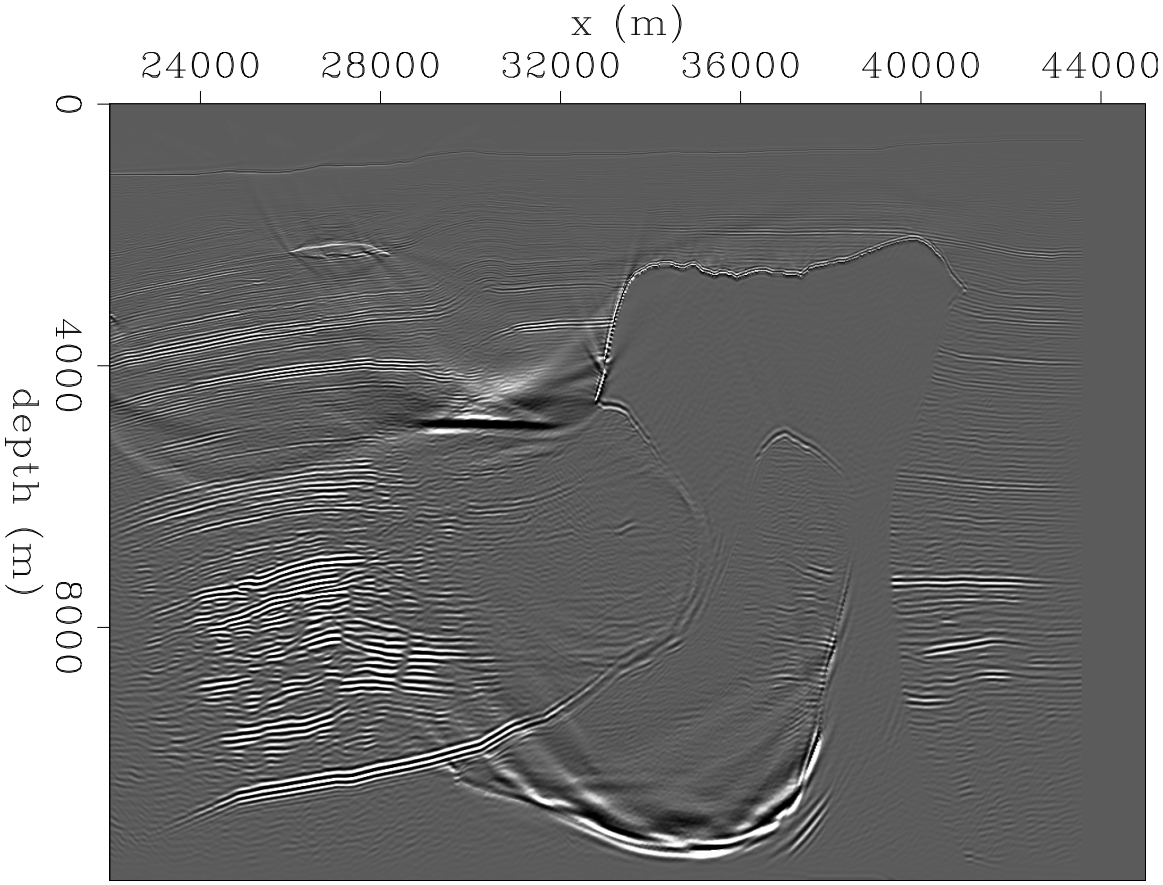

Figure 4: Compensated image using two-way reverse-time Q migration. The result shows the image at the lower region is not well compensated because of the weak updating of the Q model there. But the other events alongside the salt flank are compensated. [**CR**]

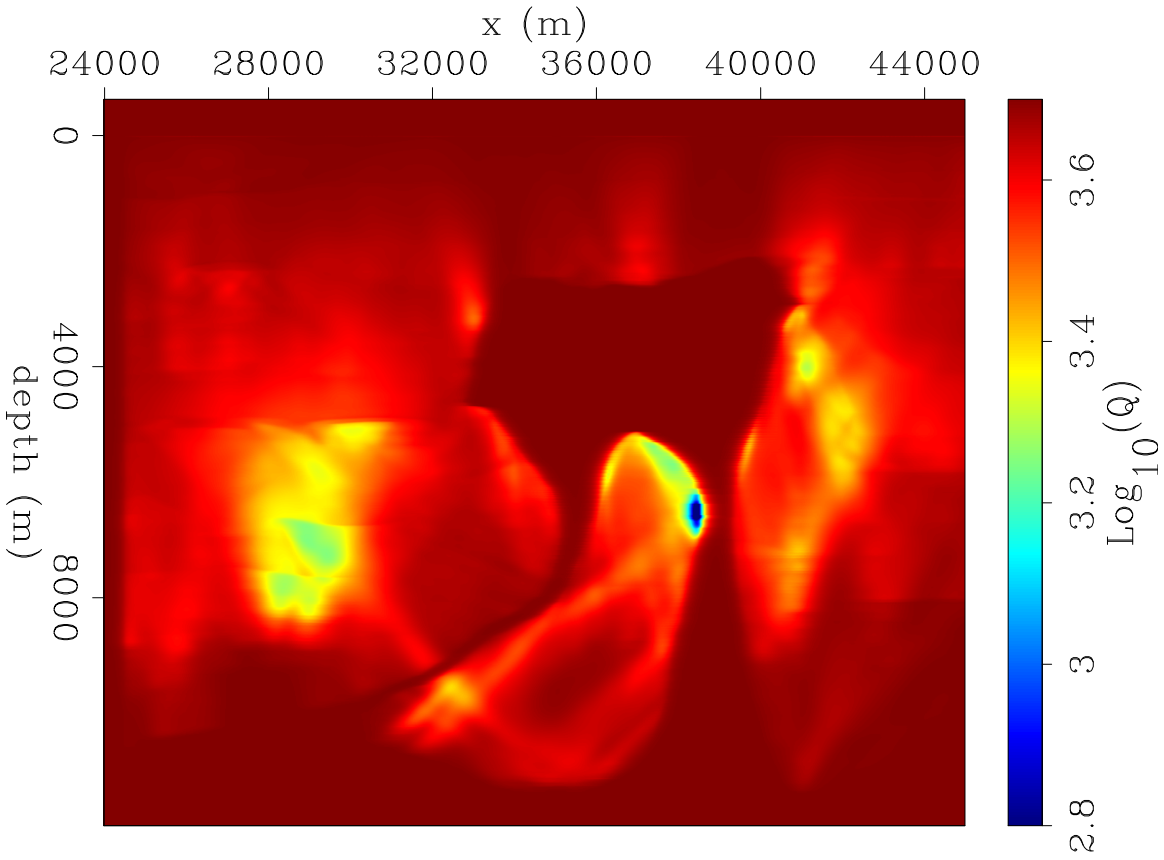

Figure 5: The inverted Q model using one-way wave-equation migration Q analysis. The result fails to resolve the Q model in the area besides the salt flank, because one-way propagation is not able to accurately reflect the steep structure. [**CR**]

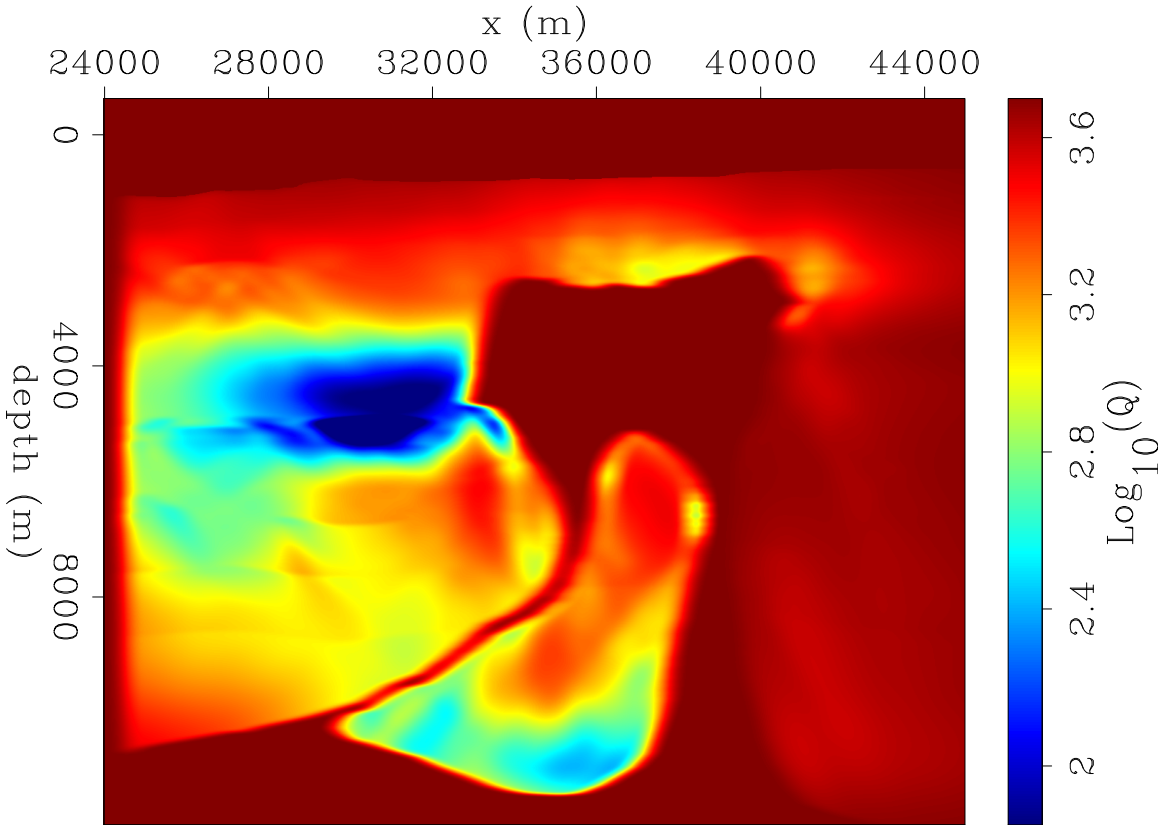

Figure 6: The inverted Q model using two-way wave-equation migration Q analysis. The result retrieves the Q model in the reservoir region beside the salt well; especially near the upper part of the salt flank. However, it still fails to update the Q model near the lower part of the salt flank because of the high-frequency image artifacts at that area. [**CR**]

CONCLUSION

This report has presented a new wave-equation migration Q analysis based on a two-way wavefield continuation method. When compared with previous work that uses a one-way downward-continuation method, the two-way based method is better in handling the steep structures, e.g. salt flanks. Numerical tests on a complex model with a salt body demonstrate the effectiveness of this two-way method on handling the overturned wave propagation caused by steep structures.

ACKNOWLEDGMENTS

The authors thank Biondo Biondi and Robert Clapp for their advice and suggestions, Schlumberger and BP for providing the 2D synthetic dataset, Yaxun Tang and Ali Almonin for help with programming, and Stanford Exploration Project sponsors for their financial support. The second author wish to thank the Jackson Distinguished Postdoctoral Fellowship at the University of Texas at Austin.

REFERENCES

Billette, F. and S. Brandsberg-Dahl, 2005, The 2004 BP velocity benchmark: 67th Conference and Exhibition, EAGE, Extended Abstracts, B035.

Cavalca, M., R. P. Fletcher, and M. Riedel, 2013, Q-compensation in complex media – ray-based and wavefield extrapolation approaches: 83rd Annual International Meeting, SEG, Expanded Abstracts, 3831–3835.

Kjartansson, E., 1979, Constant Q wave propagation and attenuation: Journal of Geophysical Research, **84**, 4737–4748.

Shen, Y., B. Biondi, R. Clapp, and D. Nichols, 2013, Wave-equation migration Q analysis (WEMQA): EAGE Workshop on Seismic Attenuation Extended Abstract.

———, 2014, Wave-equation migration Q analysis (WEMQA): SEG Technical Program Expanded Abstracts.

Zhu, T. and J. Harris, 2014, Modeling acoustic wave propagation in heterogeneous attenuating media using decoupled fractional Laplacians: Geophysics, **79**, no. 3, T105–T116.

Zhu, T., J. Harris, and B. Biondi, 2014, Q-compensated reverse-time migration: Geophysics, **79**, no. 3, S77–S87.